Reactive sputter deposition of metal oxide nanolaminates

2008 J. Phys.: Condens. Matter 20 264006

(http://iopscience.iop.org/0953-8984/20/26/264006)

J. Phys.: Condens. Matter **20** (2008) 264006 (11pp) doi:10.1088/0953-8984/20/26/264006

Reactive sputter deposition of metal oxide nanolaminates

Carolyn Rubin Aita

Advanced Coatings Experimental Laboratory, College of Engineering and Applied Science, University of Wisconsin-Milwaukee, Milwaukee, WI 53201, USA

E-mail: aita@uwm.edu

Received 19 November 2007, in final form 28 February 2008
Published 9 June 2008
Online at stacks.iop.org/JPhysCM/20/264006

Abstract

We discuss the reactive sputter deposition of metal oxide nanolaminates on unheated substrates using four archetypical examples: ZrO_2–Al_2O_3, HfO_2–Al_2O_3, ZrO_2–Y_2O_3, and ZrO_2–TiO_2. The pseudobinary bulk phase diagrams corresponding to these nanolaminates represent three types of interfaces. I. Complete immiscibility (ZrO_2–Al_2O_3 and HfO_2–Al_2O_3). II. Complete miscibility (ZrO_2–Y_2O_3). III. Limited miscibility without a common end-member lattice (ZrO_2–TiO_2). We found that, although reactive sputter deposition is a far-from-equilibrium process, thermodynamic considerations strongly influence both phase formation within layers and at interfaces. We show that pseudobinary phase diagrams can be used to predict interfacial cation mixing in the nanolaminates. However, size effects must be considered to predict specific structures. In the absence of pseudoepitaxy, size effects play a significant role in determining the nanocrystalline phases that form within a layer (e.g. tetragonal ZrO_2, tetragonal HfO_2, and orthorhombic HfO_2) and at interfaces (e.g. monoclinic (Zr, Ti)O_2). These phases are not *bulk* standard temperature and pressure phases. Their formation is understood in terms of self-assembly into the lowest energy structure in individual critical nuclei.

1. Introduction

Reactive sputter deposition is widely used for growing single layer metal oxide films on unheated substrates. Commercial advantages of reactive sputter deposition over many other oxide film growth techniques include that it is environmentally friendly and it can easily be scaled up for large area coverage. This deposition technique involves growth on a substrate in contact with a low pressure glow discharge (plasma) containing oxygen. Atoms and simple molecules are ejected from a target surface under particle bombardment and travel through the discharge to the substrate. Growth occurs under nonequilibrium conditions. The high supersaturation of adsorbed species cannot be quenched before the arrival of the next monolayer and only limited surface diffusion of the sputtered flux and oxygen species is possible on unheated substrates. Even under these conditions of a high flux and low growth temperature, oxides that do not have structural complexity in bulk [1] tend to form crystalline structures in sputter deposited films [2]. This feature of certain sputter deposited metal oxides can be combined with a nanolaminate architecture to grow technologically interesting nanocrystalline metal oxide phases that cannot be produced in single layer films.

The fundamental physiochemical issue of metal oxide nanolaminate growth is that of growth of an overlayer on a dissimilar oxide under kinetically constrained conditions [3]. Thermodynamics tells us where the system wants to end up when rate considerations are no longer of consequence. In the limit of the kinetic constraints imposed by a high arrival flux and low surface diffusion, a relevant question to ask is how important thermodynamic considerations are in determining the phase and structure within an individual layer and at its interfaces with adjacent layers.

The experimental results presented in this paper show that thermodynamics plays an important role in phase formation and in fact allows us to make predictions about the type of intralayer and interfacial structures formed. In the length scale of a nanometer, the timescale over which diffusion must occur to form the thermodynamically favored (i.e. lowest energy) structure in a just stable critical nucleus is very small. As discussed by Tromp and Hannon [4], collective phenomena such as self-assembly in individual critical nuclei become possible on this timescale.

ZrO_2–Al_2O_3, ZrO_2–Y_2O_3, ZrO_2–TiO_2, and HfO_2–Al_2O_3 nanolaminates are used for the sake of illustration in this paper. Of these individual constituents, all but Al_2O_3, which has

structural complexity, form intralayer nanocrystalline phases. Due to the extremely small crystallite size in a nanolaminate layer, these phases may not be the standard temperature and pressure (STP) phases found in equilibrium phase diagrams for the corresponding bulk binary oxides, and are hence termed 'metastable'. (This term is somewhat of a misnomer, however, because the structure under question may actually be the stable structure in a small crystallite of the binary oxide.)

There are several ways in which the nanoscale size of a crystallite can affect its structure. (I) The finite crystal size effect considers a balance between the surface and volume contributions to the Gibbs free energy of formation [5]. As the crystallite size becomes smaller, the ratio of the surface-to-volume free energy becomes larger, thus effecting a phase change. (II) The Gibbs–Thomson effect considers the increased hydrostatic pressure above a curved surface compared to a flat surface [6]. Hence, high pressure phases can form in tiny crystallites. (III) A surface dipole repulsion mechanism results in an *expanded* lattice and ultimately a phase change to a structure of higher symmetry with decreasing crystal size [7]. All of these effects are observed in nanocrystalline oxides.

Although size effects make it difficult to predict intralayer binary oxide phases on the basis of bulk binary oxide phase diagrams, we found that different types of interfaces in the nanolaminates can be predicted on the basis of bulk *pseudobinary* phase diagrams. To illustrate this point, the four nanolaminates we have chosen as examples have different propensities for forming mixed cation phases in bulk.

The bulk ambient pressure, temperature–composition phase diagrams show that the end members of ZrO_2–Al_2O_3 [8] and HfO_2–Al_2O_3 [9] pseudobinaries are immiscible, and therefore one might expect no interfacial mixed cation structures at the nanolaminates of these partners. At the other extreme, ZrO_2 and Y_2O_3 are mutually soluble and furthermore share a cubic lattice structure that changes space group from fluorite to bixbyite (the equilibrium phase of Y_2O_3) with increasing Y content over a wide composition range [10–13]. Consequently, a mixed cation cubic structure at a ZrO_2–Y_2O_3 nanolaminate's interface is predicted.

The bulk temperature–composition ZrO_2–TiO_2 pseudobinary is more complex than those of the other exemplary nanolaminates. None of the ambient pressure (Zr, Ti)-oxide phases share a lattice structure with the ambient pressure phases of ZrO_2 or TiO_2 [14–17]. Although thermodynamics predicts a driving force for the formation of mixed cation compounds and solid solutions with complex superlattice structures, there is no obvious kinetic path to achieve these structures in nanolaminates via the formation of an interfacial crystalline substitutional solid solution. On this basis, one can predict the formation of an extended complex mixed cation interfacial structure as a means of accommodating changes in stoichiometry [18]. As we shall see in section 3.3, ZrO_2–TiO_2 nanolaminates also offer a surprise: a high pressure crystalline monoclinic (Zr, Ti)O_2 phase [19–21] stabilized by the Gibbs–Thomson effect as part of their complex interfaces.

In addition to being of scientific interest, these nanolaminate systems have technical importance. Bulk ZrO_2 at atmospheric pressure crystallizes in three phases with increasing temperature: monoclinic (m-ZrO_2) to ∼1075 °C, tetragonal (t-ZrO_2) to 2360 °C, and cubic (c-ZrO_2) to the liquidus at 2680 °C [8]. Thin films of the high temperature ZrO_2 polymorphs are especially interesting. Undoped tetragonal ZrO_2 is the active component of bulk transformation-toughening ceramics (TZC), coined 'ceramic steel' by Garvie *et al* [22] because of their high fracture toughness. The first TZC films [23–26] were stacks of alternating nanocrystalline t-ZrO_2 and amorphous Al_2O_3 layers, each several nanometers thick. These 'smart' nanolaminates offer excellent active protection against pitting corrosion of stainless steel compared to passive single layer or multilayer coatings [27]. The biocompatibility of TZC films makes them candidates for protection of indwelling biomedical devices in the harsh environment of bodily fluids [28]. In addition, their combined optical transparency well into the far ultraviolet spectrum [29, 30], thermal stability [30], and reasonable hardness [26] make them candidates for optical coatings in a variety of harsh environments.

Bulk 'cubic stabilized ZrO_2' is a family of hard, refractory materials, stabilized at room temperature by the addition of +3 valence metals, chiefly Y [8]. Yttria-stabilized cubic zirconia (YSZ) thin films have been traditionally used for hard, highly transparent, high refractive index optical coatings [31].

ZrO_2–TiO_2 nanoarchitectured alloys are photoactive materials. Their photocatalytic [32, 33], photoluminescent [34], photon-enhanced thermoluminescent [35], and cathodoluminescent [36] behavior has been the subject of sustained research. ZrO_2–TiO_2 nanolaminates are high optical refractive index solids [37]. In addition, significant optical absorption in ZrO_2–TiO_2 nanolaminates is tunable over the ultraviolet spectrum from 3.61 to 5.70 eV by varying the ZrO_2/TiO_2 ratio in a bilayer [38].

Thin films of non-monoclinic HfO_2 phases are of interest as a replacement gate dielectric for SiO_2 in complementary metal–oxide–semiconductor devices [39]. Furthermore, tetragonal HfO_2 has also been considered as the active component in transformation-toughening ceramics based on a stress-induced t → m transformation [40], analogous to this phenomenon in ZrO_2. As we shall see in section 3.4, non-monoclinic HfO_2 phases can be formed using a HfO_2–Al_2O_3 nanolaminate architecture to truncate HfO_2 crystallite growth.

In section 2, we very briefly discuss several basic factors to consider when using reactive sputter deposition to reproducibly tailor an oxide structure. The examples given are from our work using a radio frequency excited diode sputter deposition apparatus. The considerations we present, however, are of general concern independent of the type of reactor used. In section 3, we describe the intralayer and interfacial characteristics of the exemplary nanolaminate systems mentioned above. We conclude with general observations of these systems as archetypes in section 4 and use these observations to predict interfacial and intralayer structures in several nanolaminates with other oxide partners. Lastly, we present several future directions for investigation.

2. Reactive sputter deposition of metal oxides: several basic considerations

The nanolaminates discussed here are grown by sequential reactive sputter deposition from metal targets using automated radio frequency excited diode configuration reactors. The essential sputtering deposition reactor consists of two electrodes separated by a small distance. The target is placed over the cathode. The substrates are placed on the anode. A high negative potential is applied to the cathode and a self-sustained discharge or plasma is established [41]. A luminescent field free negative glow fills most of the region between the electrodes. Physical sputtering occurs when positive gas ions from the negative glow enter the cathode sheath, are accelerated in the cathode field and strike the target surface. Target atoms and small molecules are ejected primarily by momentum transfer during a collision cascade [42]. Most of the sputtered species are uncharged, assume a random motion between the electrodes, and condense on any surface in their path, e.g. the substrate.

A small amount of O_2 introduced into a rare gas discharge is gettered by the metal target surface and a metal oxide surface layer forms. However, the ballistic nature of the sputtering process simultaneously dissociates this reacted target layer. The state of target oxidation is a dynamic balance between compound formation and dissociation for a given set of machine parameters. The sputtered flux in general consists of target atoms, M, and molecular oxide complexes, MO_x, where x is usually unity [43]. In most cases, further oxidation of the sputtered flux must occur at the substrate in order to form the highest valence metal oxide film.

In an rf diode deposition system, two features of the plasma play a key role in determining phase formation and orientation in a sputter deposited oxide film: (1) the relative flux of M and MO_x species arriving at the substrate and (2) oxygen in any form available for reaction at the substrate [2]. These features depend upon several easily controllable machine process parameters, namely, the amount of O_2 introduced into a rare gas discharge, the applied cathode voltage, and the type of rare gas used in conjunction with O_2.

'Phase maps' guided the selection of deposition parameters used to grow each type of layer. These process parameter–plasma chemistry–film structure maps were developed for single layer metal oxide film growth and used in conjunction with plasma diagnostics to obtain a desired metal oxide phase independent of a specific reactor [43]. For example, figure 1 shows a phase map for deposition from a Zr target sputtered in Ar–O_2 discharges. The observed phases are mapped on process parameter space (the gas O_2 content and applied cathode voltage). In addition, the set of parameters at which oxygen in any form is observed in the discharge is indicated by a dashed line. For a fixed cathode voltage, the solid lines indicate the fractional flux of Zr, $f(\mathrm{Zr})$, in the plasma where $f(\mathrm{Zr}) + f(\mathrm{ZrO}) = 1$.

Figure 1 shows that a large Zr fractional flux and the absence of oxygen in the discharge for further reaction at the substrate results in metal films. A small Zr fractional flux and the absence of oxygen in the discharge results in ZrO, a suboxide. Data [44] show that the deposition rate has not significantly decreased under these conditions, i.e., the deposition is still in 'metallic mode.' However in an rf diode system, the formation of the highest valency oxide, ZrO_2, is associated with a small or vanishing Zr fractional flux *and* excess O in the discharge. This result applies to other metal–oxygen systems as well, regardless of whether a metal or oxide target is used [2]. In addition, films grown under these conditions are likely to have individual crystallites in their low energy configuration. Namely, in the absence of strong adatom–substrate interaction, the closest-packed crystal planes of a crystallite grow parallel to the growth interface [45].

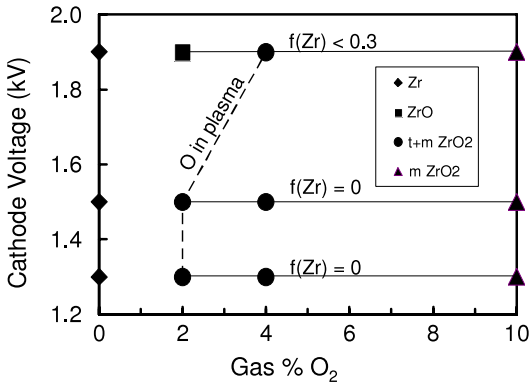

Figure 1. A phase map for deposition from a Zr target sputtered in Ar–O_2 discharges. The observed phases are mapped on process parameter space (the gas O_2 content and applied cathode voltage). In addition, the set of parameters at which oxygen in any form in observed in the discharge is indicated by a dashed line. For a fixed cathode voltage, the solid lines indicate the fractional flux of Zr, $f(\mathrm{Zr})$, in the plasma where $f(\mathrm{Zr}) + f(\mathrm{ZrO}) = 1$.

Although not observed in the Zr–O phase map, in some cases (i.e. the Y–O phase map [2, 43]) both a large metal flux and excess oxygen are observed in the discharge. In this situation, the resulting films are likely to have orientational and/or compositional disorder.

3. Examples of sputter deposited metal oxide nanolaminates

3.1. ZrO_2–Al_2O_3 nanolaminates

Our initial motivation for studying ZrO_2–Al_2O_3 nanolaminates was to fabricate a smart transformation-toughening coating. Transformation-toughening in bulk ZrO_2 is based on the principle that an advancing crack triggers a local t $\rightarrow$ m ZrO_2 transformation at its tip. As a consequence, a defect structure is set up at the crack tip that hinders further crack growth [8]. In order to be transformation-toughening, a ZrO_2 film must have a large volume fraction of t-ZrO_2 nanocrystallites that will locally transform in response to localized stress [23].

A phase map of the sputter deposited Zr–O system (figure 1) shows that single layer ZrO_2 films contain either the monoclinic phase or are biphasic, containing both monoclinic and tetragonal phases. In biphasic films, t-ZrO_2 formation is associated with small crystallites. We surmised that 'pure' t-ZrO_2 (without m-ZrO_2) could be captured by limiting crystallite growth. To this end, we used a nanolaminate

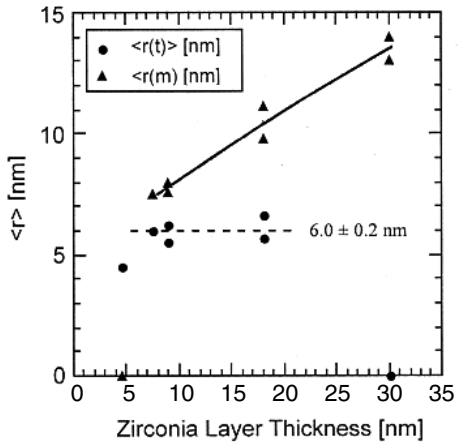

Figure 2. The average t-ZrO_2 and m-ZrO_2 crystallite dimension perpendicular to the substrate as a function of ZrO_2 layer thickness in ZrO_2–Al_2O_3 nanolaminates [26].

structure of ZrO_2 and amorphous Al_2O_3. The Al_2O_3 layers served two purposes: first as ZrO_2 growth truncation and restart surfaces, and second as a mechanical constraint on the 'softer' ZrO_2 layers at the time of a t $\rightarrow$ m ZrO_2 during film service.

Double angle x-ray diffraction (XRD) showed that the ZrO_2 phase composition changed from solely t-ZrO_2 to t + m-ZrO_2 with increasing ZrO_2 layer thickness in the nanolaminates [24]. The films were textured such that t-ZrO_2 {111} and m-ZrO_2 $(11\bar{1})$ planes (when present) grew parallel to the substrate. These are the closest-packed orientations, and are expected when there is weak adsorbate–substrate interaction compared to the interaction among adsorbed species [45]. Figure 2 shows the average t-ZrO_2($\langle r(\mathrm{t})\rangle$) and m-$ZrO_2$ ($\langle r(\mathrm{m})\rangle$) crystallite size in the growth direction, calculated from x-ray diffraction line broadening, as a function of ZrO_2 layer thickness [25, 26]. We see that $\langle r(\mathrm{t})\rangle$ saturates at 6.0 ± 0.2 nm, whereas $\langle r(\mathrm{m})\rangle$ continues to increase as a function of ZrO_2 layer thickness.

The behavior shown in figure 2 is consistent with a finite crystal size effect in which t-ZrO_2 crystallites initially form and subsequently transform to m-ZrO_2 as they grow beyond 6 nm. The Gibbs free energy accompanying a t $\rightarrow$ m ZrO_2 growth transformation is given by

$$\Delta G = Ar^3\Delta g + Br^2\Delta\gamma, \tag{1}$$

where Δg is the change in volume free energy, $\Delta\gamma$ is the change in surface free energy, r is a characteristic dimension of the crystallite, and A and B are geometric factors describing the crystallite's shape. At the point of transformation, $\Delta G = 0$, and the corresponding critical dimension, $r = r_c$ can be calculated from a balance of the volume and surface energy terms. High resolution transmission electron microscopy (HRTEM) showed that ZrO_2 crystallites were approximately rectangular in shape with a height r in the growth direction and a base $2r$ in the substrate plane [26]. For this geometry, an end-point thermodynamics calculation yields $r_c = 3.79[1 - (T/1448\ \mathrm{K})]^{-1}$ (nm) [25, 26]. A value of $r_c = 6.2$ nm is obtained for $T = 564$ K (the growth temperature), in excellent agreement with the XRD data in figure 2.

The above results demonstrate that solely t-ZrO_2 is produced when the ZrO_2 layer thickness is $\leqslant r_c$. Now consider the transformation-toughening behavior of such a ZrO_2–Al_2O_3 nanolaminate. Figure 3 is a digitized HRTEM image of several layers adjacent to the substrate showing four ZrO_2 crystallites in various stages of t $\rightarrow$ m transformation due to the mechanical abuse during HRTEM preparation [46]. t(111) planes were aligned parallel to the substrate, whereas m$(11\bar{1})$ planes were tilted by $\sim 9°$, indicating an out-of-plane rotation, which is the signature of a t-ZrO_2 crystallite undergoing a stress-induced transformation. However, unlike the product of a growth transformation, examination of many crystallites showed that the stress transformation product was highly distorted.

Electron beam irradiation experiments [47] showed significant superplasticity, manifested by 'adjustments' in t-ZrO_2 interplanar spacings and angles. Figure 4 shows a t-ZrO_2 crystallite in which a transformation has been initiated by a mild dose of irradiation. Note that the surrounding Al_2O_3 layers are intact. Figure 5 shows the lattice spacing of crystallites as a function of electron beam dose, indicating that *plastic* deformation continued within t-ZrO_2 layers as the dose was increased. In fact, only under radiation conditions severe enough to punch holes in the Al_2O_3 layers did a transformation to the expected values for interplanar spacing of m-ZrO_2 occur. This nanoscale superplasticity of t-ZrO_2 in ZrO_2–Al_2O_3 nanolaminates is very different from the martensitic transformation-toughening mechanism of the corresponding bulk ceramic material [8].

3.2. ZrO_2–Y_2O_3 nanolaminates

The standard temperature and pressure (STP) phase of Y_2O_3 has cubic bixbyite lattice structure [10–13]. There are two nonequivalent positions for Y in the Y_2O_3 unit cell. A phase map for the Y–O system indicates the plasma characteristics for which site-ordered Y_2O_3 is grown [2, 43]. Process parameters that produce these characteristics were chosen here to produce site-ordered nanocrystallites in the Y_2O_3 layers. The idea was to use these Y_2O_3 nanocrystallites as templates for c-ZrO_2 growth, i.e. to produce nanolaminates with nanoepitaxial pseudomorphic c-ZrO_2 layers assisted by interfacial YZO formation.

Films on fused SiO_2 in which the nominal ZrO_2 layer thickness, X, ranged from 4 to 30 nm and the nominal Y_2O_3 (template) layer thickness was held constant at 4 nm were studied by XRD and HREM [48]. The first layer adjacent to the substrate was c-Y_2O_3. Two major peaks, denoted I and II, were observed from XRD data. Figure 6(a) shows the interplanar spacing corresponding to these peaks as a function of the nominal ZrO_2 layer thickness. Peak I is present in films with X from 4 to 18 nm. The lattice spacing corresponding to peak I lies between that of (111) t-ZrO_2 planes and (222) c-Y_2O_3 planes. We conclude that the structure responsible for peak I is c-(ZYO). Peak II is present in films with X from

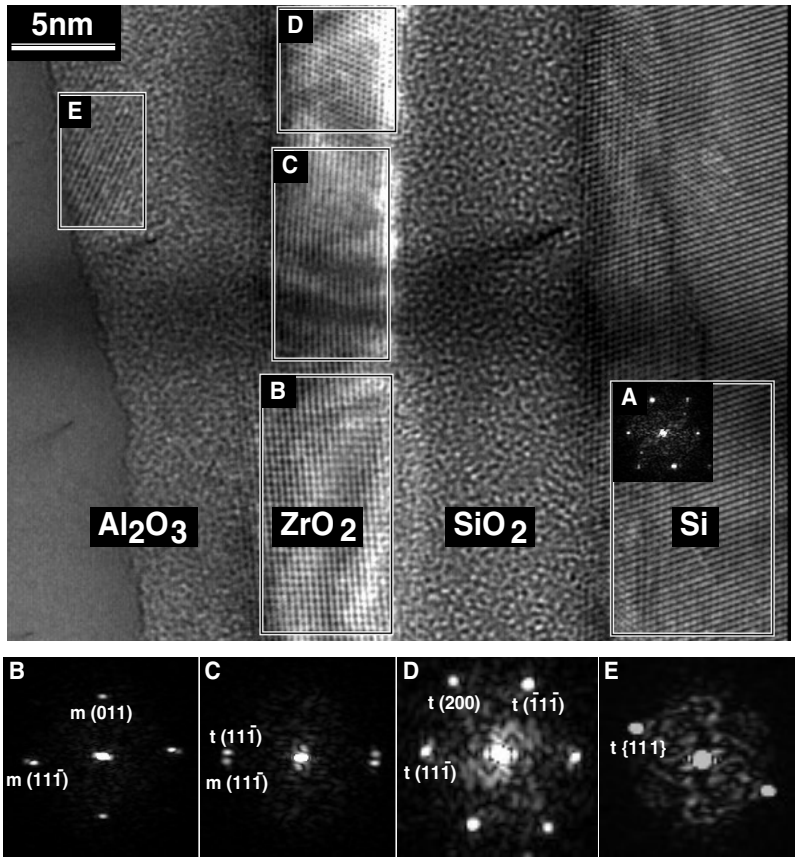

Figure 3. Digitized HRTEM image of several layers adjacent to the substrate showing four ZrO_2 crystallites in various stages of transformation due to the mechanical abuse during HRTEM preparation [47].

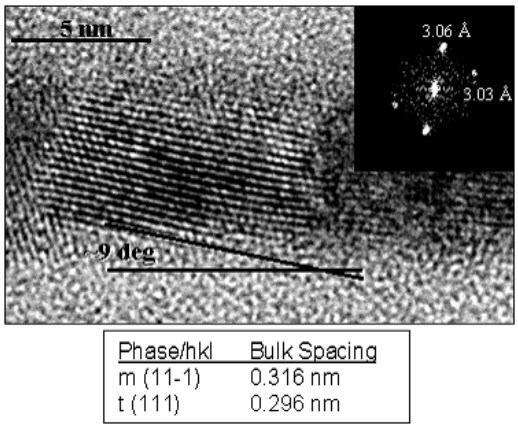

Figure 4. Digitized HRTEM image with diffractogram of a single t-ZrO_2 crystallite that is beginning to transform after being subjected to a mild dose of electron beam irradiation [47].

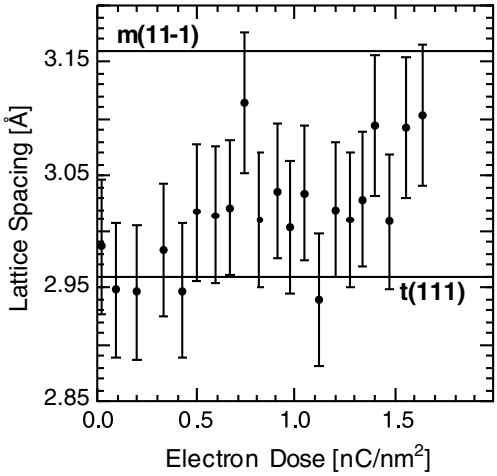

Figure 5. Lattice spacing of crystallites in 5 nm thick ZrO_2 layers as a function of electron beam dose [47].

12 to 30 nm. The lattice spacing corresponding to peak II is identical to that of the (11$\bar{1}$) planes of m-ZrO_2. Another point seen from figure 6(a) is that m-ZrO_2 does not form in small crystallites, consistent with the results from ZrO_2–Al_2O_3 nanolaminates discussed above.

The average crystallite size, $\langle r \rangle$, of cubic and monoclinic crystallites perpendicular to the substrate determined from XRD line broadening is shown as a function of X in figure 6(b). A dashed line indicates the values that would have been obtained if the average crystallite size equaled the ZrO_2 layer thickness. A striking feature about these data is that $\langle r(c) \rangle$ is *greater* than X for $X = 4$–6 nm. These data show that for small bilayer periodicity a c-(Zr, Y) oxide crystallite spans several layers before renucleation events occur. Cross-sectional HREM images concur with this conclusion.

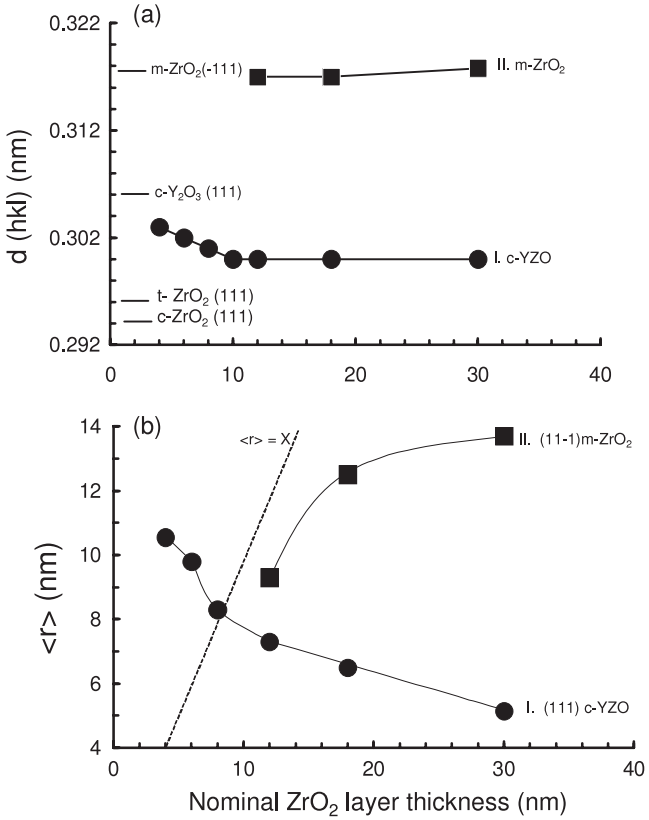

Figure 6. (a) Interplanar spacing of (111) c-(Zr,Y)-oxide and (11$\bar{1}$) m ZrO_2 as a function of ZrO_2 layer thickness in ZrO_2–Y_2O_3 nanolaminates on fused SiO_2 substrates. (b) Average c-ZrO_2 and m-ZrO_2 crystallite dimension perpendicular to the substrate as a function of ZrO_2 layer thickness in ZrO_2–Y_2O_3 nanolaminates. A diagonal line indicates a crystallite size equal to the ZrO_2 layer thickness.

3.3. ZrO_2–TiO_2 nanolaminates

ZrO_2–TiO_2 nanolaminates with different overall chemistry are good candidates for a family of films with high transparency, a large dielectric constant, and with an optical absorption edge that is tunable across much of the ultraviolet spectrum. In such a structure, tailored optical absorption can potentially be achieved though changes in bilayer architecture. The onset of optical absorption in the end members was experimentally determined to be ∼5 eV for ZrO_2 polymorphs [29, 49–51] and ∼3 eV for TiO_2 polymorphs [52]. The absorption onset of pseudobinary $(ZrO_2)_x$–$(TiO_2)_{1-x}$ structures with different stoichiometry could therefore conceivably span an ultraviolet wavelength range from 248 to 414 nm. In addition, Zr and Ti atoms have the same electronegativity, 1.6 [53], and also form d^o oxides (ZrO_2 and TiO_2) with isovalent cations, Zr^{+4} and Ti^{+4}. This electronic similarity theoretically permits the substitution of one cation for the other in dilute solution [54, 55] with minimal electronic disturbances at a nanolaminate interface.

Although ZrO_2 and TiO_2 are electronically compatible, there is a potential complication when combining them in an engineered structure. There is a large difference in the ionic radii of Ti^{+4} (0.68 Å) and Zr^{+4} (0.80 Å) [56]. Consequently, ambient pressure ZrO_2 and TiO_2 crystals do not share a common lattice structure. So although bulk thermodynamic considerations indicate a driving force for chemical mixing [14–17], there is no obvious kinetic path to achieve it via formation of an extensive crystalline substitutional solid solution (i.e. $Zr_xTi_{(1-x)}O_2$ where $0 \leqslant x \leqslant 1$ with a single lattice type does not form).

We previously reported that the optical absorption coefficient, $\alpha(E)$, of a series of ZrO_2–TiO_2 nanolaminates does indeed systematically change as a function of bilayer architecture [38]. However, the results could not be adequately explained by either an amalgamation model, which involves formation of a continuous $Zr_xTi_{(1-x)}O_2$ solid solution, or a persistence model, which involves complete phase separation to form a $(ZrO_2)_x$–$(TiO_2)_{(1-x)}$ mixture [57]. Instead, we developed a microscopic model that takes into account Zr–O–Ti linkages adjacent to an extended interfacial region. In this sense, ZrO_2–TiO_2 nanolaminates are archetypical of other oxide partners with important optical behavior, in which there is neither complete miscibility nor immiscibility of the end members.

To understand the complex nature of interfaces in ZrO_2–TiO_2 nanolaminates, we next focus on the behavior of two architectures with ultrathin bilayers: (A) 1.5 nm ZrO_2–1.5 nm TiO_2 and (B) 4.0 nm ZrO_2–1.5 nm TiO_2. Architecture A did not yield XRD peaks. Architecture B showed a major peak attributed to diffraction from the (11$\bar{1}$) planes of an extensive *monoclinic* $(ZrTi)O_2$ solid solution. This structure, reported in thin films in [58] for the first time, is isomorphic with m-TiO_2, that naturally occurs in rocks [19, 20], and m-$ZrTiO_4$, that is produced by applying high hydrostatic pressure to orthorhombic $ZrTiO_4$ powder [21].

The Raman spectra of architectures A and B is shown in figure 7 [38, 58]. In addition to features associated with short range order in rutile TiO_2, these spectra show several important non-rutile features. (1) All features between 700 and 900 cm^{-1} not assigned to rutile TiO_2 are attributable only to Zr–O–Ti bonding and not to any ambient or high pressure ZrO_2 or TiO_2 phase [58–61]. These features include the slightly elevated background in architecture A and the broad peak in architecture B above 700 cm^{-1} with local maxima at 800 and 875 cm^{-1}. These local maxima are characteristic of α-PbO_2 type orthorhombic $(Zr, Ti)O_2$ [61]. (2) The shoulder at 180 cm^{-1} in architecture B is attributed to short range order in m-$(Zr, Ti)O_2$, which is isostructural with m-ZrO_2 [62].

These results are consistent with a complex and extended structure at a ZrO_2-on-TiO_2 interface in the nanolaminates to accommodate chemical mixing without the path of heteroepitaxy observed in ZrO_2–Y_2O_3 nanolaminates. This structure, shown schematically in figure 8, consists of several components: a nanocrystalline TiO_2 phase based on a defect rutile structure expected to form in pure TiO_2 for the given deposition conditions [61, 62] but here doped with Zr, followed by an amorphous Zr,Ti oxide phase with yet-to-be determined short range order (architecture A), followed by an amorphous phase with α-PbO_2 type short range order, followed by an extensive crystalline m-$(Zr, Ti)O_2$ solid solution (architecture B). Films with ZrO_2 layer thickness greater than the 4 nm

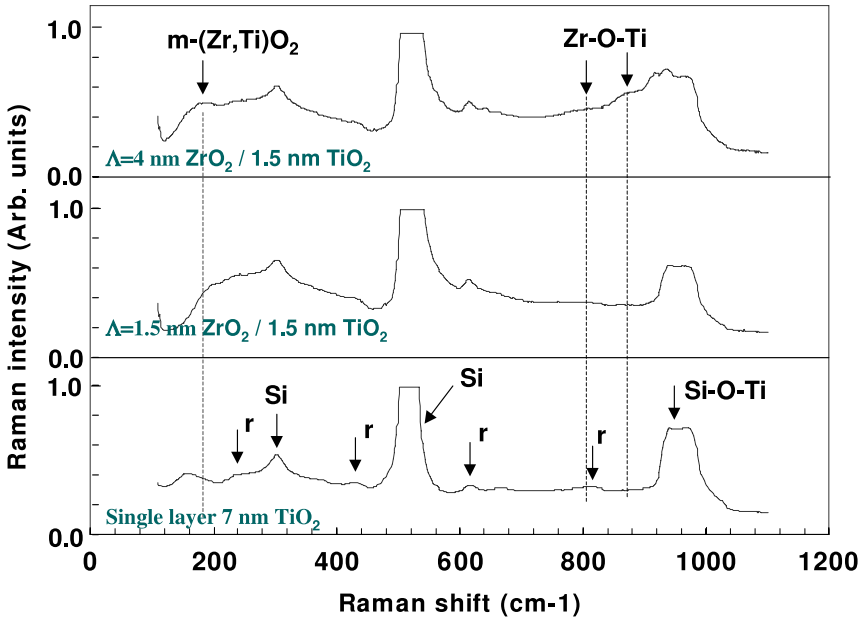

Figure 7. Raman spectra of ZrO_2–TiO_2 nanolaminates and a 7 nm thick TiO_2 monolithic film [58].

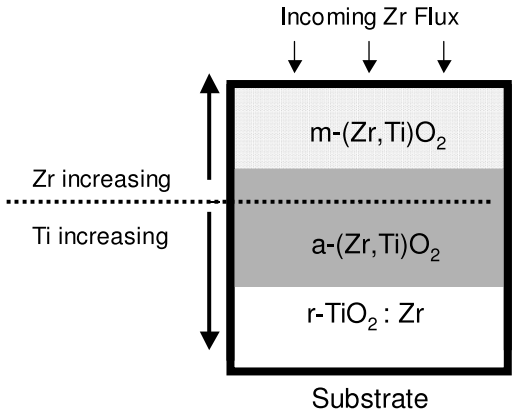

Figure 8. A schematic drawing of the development of an interfacial structure as Zr flux is deposited on a TiO_2 underlayer. The notation 'r-TiO_2:Zr' indicates that the TiO_2 layer with rutile short range atomic order has received some Zr doping as a result of cation mixing, and 'a-(Zr, Ti)O_2' and 'm-(Zr, Ti)O_2' are, respectively, amorphous and crystalline mixed cation structures. The nominal interface is indicated by a dashed line [58].

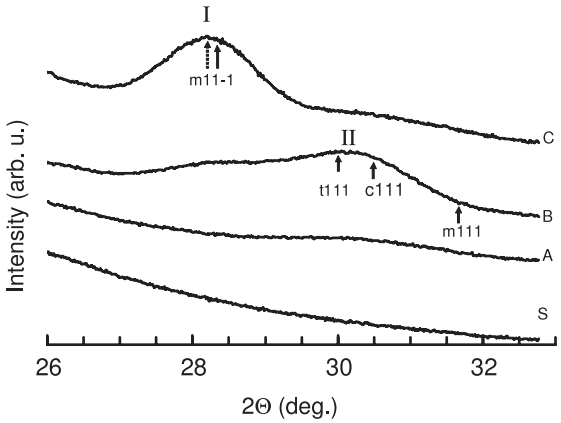

Figure 9. XRD patterns of the HfO_2–Al_2O_3 films (architectures given in table 1) on fused silica substrates and a bare substrate (S). The dashed arrow indicates the position of the m(11$\bar{1}$) peak centroid. Solid arrows indicate the position for m{11$\bar{1}$}, m{111}, t{111}, and c{111} planes in bulk HfO_2 [72].

architecture B first form t-ZrO_2 or c-ZrO_2 nanocrystallites (which cannot unambiguously be distinguished in this case) on top of the m(Zr, Ti)O_2 component and ultimately form m-ZrO_2.

Diffusional amorphization with subsequent recrystallization provides a mechanism for the amorphous then crystalline nature of the interface. This mechanism was first identified in metallic bilayers [63, 64]. An important feature is that the amorphous layer created by asymmetric diffusion across the interface is self-limiting in thickness, as observed in architecture B, because its growth rate ultimately competes with the heterogeneous nucleation and growth of a crystalline phase, which in this case is m-(Zr, Ti)O_2.

The unexpected feature at a ZrO_2-on-TiO_2 interface is nanocrystalline m-(Zr, Ti)O_2 with a crystallite size in the growth direction on the order of a nanometer calculated from XRD line broadening. The formation of this high pressure phase can be understood in terms of the Gibbs–Thomson effect [6], i.e. vapor pressure enhancement, p/p_o, above a crystallite of radius r, given by

$$p/p_o = \exp(2\gamma\Omega/rkT), \tag{2}$$

where γ is the surface energy and Ω is the volume of a (Zr, Ti)O_2 unit, k is Boltzmann's constant, and T is absolute temperature. The m-(Zr, Ti)O_2 crystallites (whose precise chemistry is undetermined) were estimated to have a dimension of 1.25 nm in the growth direction in architecture

Table 1. Architecture of HfO_2–Al_2O_3 nanolaminates. (Note: all architectures are $0.6HfO_2$–$0.4Al_2O_3$ by volume.)

Film	HfO_2/Al_2O_3 layer thickness (nm)	No of HfO_2/ Al_2O_3 layers	Film thickness (nm)
A	7.3/5.2	20/19	245
B	10.2/7.3	16/15	273
C	14.5/10.4	10/9	239

B [38, 58]. A calculation shows that a pressure range of 5–70 GPa corresponds to the stoichiometric endpoints from TiO_2 to ZrO_2 for a cluster of this size [38, 58].

So far we have not discussed cation mixing at a TiO_2-on-ZrO_2 interface. Given the ballistic nature of sputter deposition coupled with the thermodynamic driving force for forming zirconium titanium oxides, some amount of diffusion of an arriving Ti-bearing flux into an underlying ZrO_2 layer is expected. However, low temperature post-deposition annealing studies of both a single ZrO_2–TiO_2 bilayer [65] and ZrO_2–TiO_2 nanolaminates [66] show that the formation of an interfacial amorphous $(Zr, Ti)O_2$ alloy is chiefly due to diffusion of Zr into TiO_2, *not* by diffusion of Ti into ZrO_2.

3.4. HfO_2–Al_2O_3 nanolaminate

ZrO_2 and HfO_2 are called 'sister' materials because of their similar crystal structure and phase evolution path with increasing temperature and pressure [67]. Bulk HfO_2 at atmospheric pressure crystallizes in three phases with increasing temperature: monoclinic to 2000 K, tetragonal to 2870 K, and cubic to the compound's melting temperature at 3073 K [9, 67, 68]. In addition, bulk monoclinic (m) HfO_2 transforms to a sequence of orthorhombic (o) phases with increasing pressure [67–70].

Relatively thick (∼200–400 nm) HfO_2 films grown at room temperature by reactive sputter deposition contain solely m-HfO_2 [71]. An important question is whether m-HfO_2 is the nucleated phase, or, as in the case of ZrO_2, it is the transformation product of a nucleated non-monoclinic phase that has grown beyond a critical size. To this end, we used a nanolaminate architecture with amorphous Al_2O_3 as HfO_2 growth termination and restart layers to capture the initial stages of sputter deposited HfO_2 crystallite growth [72]. By analogy with ZrO_2–Al_2O_3 nanolaminates (section 3.1) we surmised it was possible to capture these initial stages between two Al_2O_3 layers because the bulk phase diagram of HfO_2–Al_2O_3 shows very limited mutual solid solubility [9].

HfO_2–Al_2O_3 nanolaminates were grown on unheated fused SiO_2 and the surface oxide of ⟨111⟩ Si, and their structure was studied by XRD and HREM [72]. Figure 9 shows the conventional XRD patterns obtained from the HfO_2–Al_2O_3 nanolaminates whose architecture is given in table 1. From these data, it can be seen that diffraction from m-HfO_2 decreased and diffraction from non-monoclinic HfO_2 phases increased with decreasing HfO_2 layer thickness, consistent with some kind of size effect.

HRTEM was used to study nanolaminate A, with 19 bilayers of 7.3 nm HfO_2/5.2 nm Al_2O_3 [70]. (Note that this film shows no discernable peaks in a conventional XRD scan (figure 9) and the HfO_2 constituent might be mistaken to be amorphous.) However, figure 10(a) is a HRTEM image showing lattice fringes of three nanocrystals. Diffractograms of the two larger nanocrystals, calculated from the boxed areas A and B, are shown in figure 10(b).

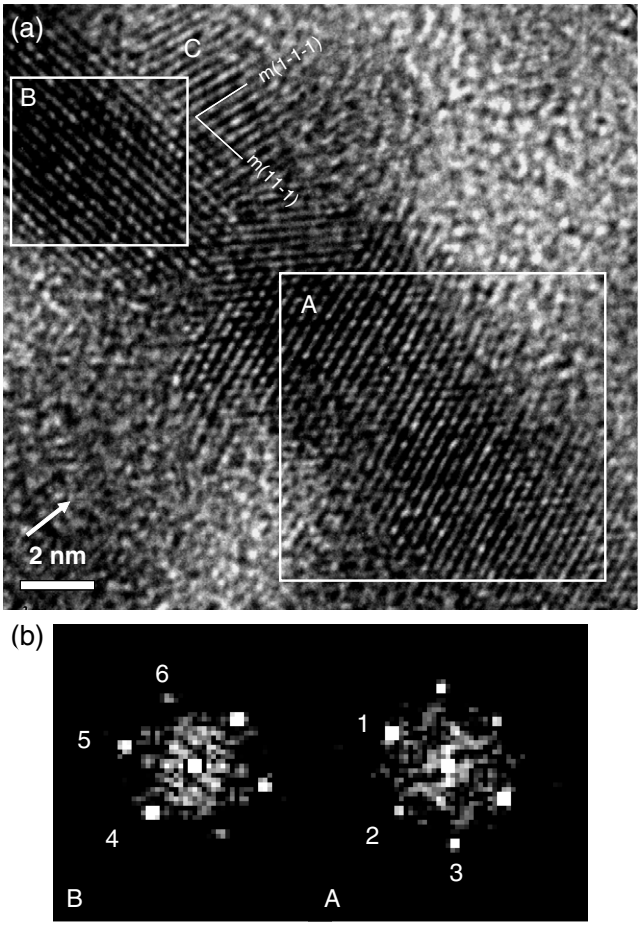

Figure 10. High magnification cross-section image of HfO_2 nanocrystallites embedded between two amorphous Al_2O_3 layers in a HfO_2–Al_2O_3 nanolaminate with 19 bilayers of 7.3 nm HfO_2/5.2 nm Al_2O_3. (b) Diffractograms of boxed image areas A (t-HfO_2) and B (m–o polysynthetic twin) [72].

The three sets of lattice fringes in area A corresponding to spots 1–3 are assigned to t-HfO_2 on the basis of spacings and interplanar angles. The tetragonal phase was the nucleated structure in ZrO_2, as well. Area B tells a different story. Spot 4 is assigned to the {111} planes of o-HfO_2 with a *Pbca* space group, a high pressure phase obtained in bulk by compressing m-HfO_2 at 4 GPa [68–70]. This phase has been unambiguously identified by Bohra *et al* [73] in HfO_2 films grown by atomic layer deposition and subsequently annealed at 1073 K. Spots 4 and 5 and spots 4 and 6 form a twinned *monoclinic* bicrystal with a (100) composition plane and a topology shown schematically in figure 11. In this scenario, the planes associated with spot 4 behave as $m(11\bar{1})$ planes, albeit with the spacing of o(111). The interplanar angle between m(111) twin planes [74] is the sum of $\phi_{o211,-211}$ and $2(\beta - \pi/2)$, where $\beta = 99.23°$ for m-HfO_2, yielding

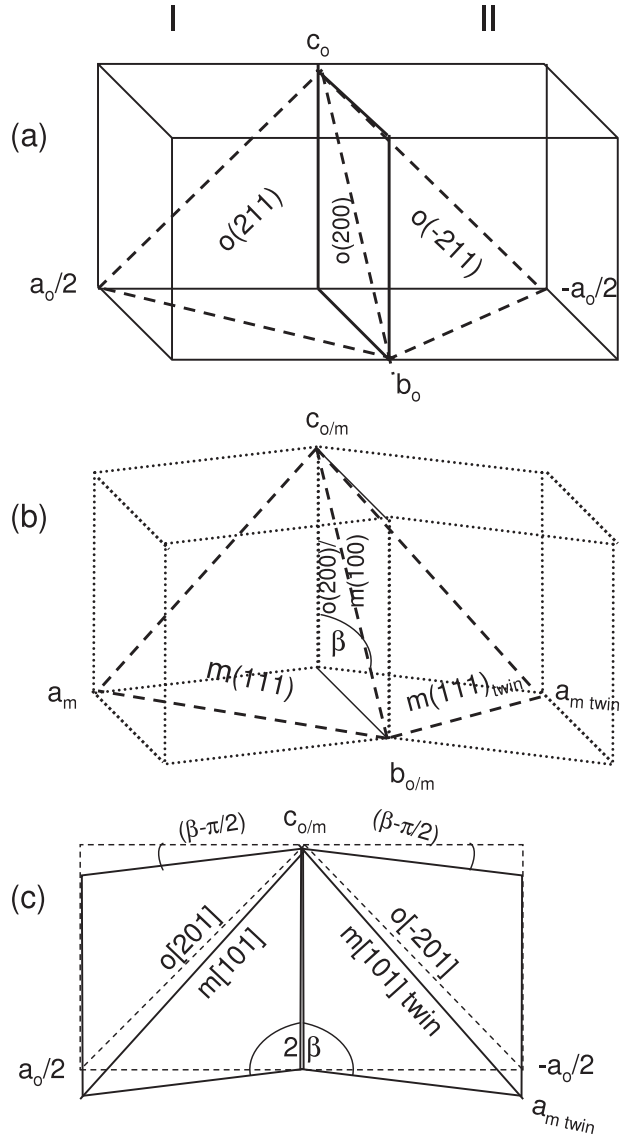

Figure 11. Schematic drawing of the relationship between an m-HfO_2 polysynthetic twin with an m(100) composition plane and the o-HfO_2 *Pbca* space group unit cell from which it is derived. (a) The o unit cell divided into two sections along the **a** axis by the o(200) plane. (b) Formation of a polysynthetic twin from sections I and II. The composition plane o(200)/m(100) and the $b_{o/m}$ and $c_{o/m}$ axes are invariant. (c) Projection along the (020) plane of the o lattice and the m twin showing angular relationships involved in the transformation (after [72]).

$\phi_{m111,111(twin)} = 45.9°$. $\phi_{m111,111(twin)}$ is reasonably close to the observed value of 51° (figure 11). Ohtaka *et al* [69] have shown that o-HfO_2 with a *Pbca* space group structure is closely related to the monoclinic $P21/c$ space group via a twinning operation of the latter. From the above analysis, we suggest that area B is in the process of undergoing the reverse of the m → o transition described by Ohtaka *et al* [69]. However, it is uncertain whether this transition has occurred during film growth or whether it is the result of the extreme stress the film experiences during HRTEM sample preparation.

Crystallite C has $d_{hkl} = 0.312$ nm, which is very close to $d_{m\{11\bar{1}\}} = 0.315$ nm. The fringes of crystallite C make an angle of 75° with those associated with spot 4 in area B. This angle, marked on the HRTEM image, is equal to the calculated value of $\phi_{m11\bar{1},1\bar{1}\bar{1}}$. We therefore conclude that crystallite C is a monoclinic outgrowth of the underlying region B, which contains both characteristics of o-HfO_2 and (twinned) m-HfO_2.

A comparison of the pre-monoclinic phases in ZrO_2 and HfO_2 shows that the high temperature tetragonal phase is initially formed in both oxides. (An end-point thermodynamics calculation cannot be carried out to quantify r_c for the t → m transformation in HfO_2 because the appropriate energy terms are unknown.) However, the formation of o-HfO_2 as an initial phase in addition to t-HfO_2 is a striking difference between ZrO_2 and HfO_2. One might surmise that o-HfO_2 phase formation is a manifestation of the Gibbs–Thomson effect, but again there is insufficient surface energy information for a supporting calculation. Lastly, it should be noted that the extent to which subtle differences in ZrO_2 and HfO_2 electronic structure [75] may play a role in the formation of the initial phases is unknown. The calculated energies/atom of the orthorhombic (*Pbca*) and monoclinic phases are considerably closer in HfO_2 than in ZrO_2, perhaps providing an additional structure for HfO_2 to access as an initial phase, along with t-HfO_2.

4. Summary and future directions

In describing reactive sputter deposition of metal oxide nanolaminates, we have for the sake of illustration focused on four archetypical examples involving *crystalline* nanostructures. We found that, although reactive sputter deposition is a far-from-equilibrium process, thermodynamic considerations strongly influence both phase formation within layers and at interfaces.

The following general observations are made from the results and discussion presented above.

(1) The pseudobinary bulk phase diagrams corresponding to the nanolaminates used as examples represent three types of interfaces. (I) Complete immiscibility (ZrO_2–Al_2O_3 and HfO_2–Al_2O_3). (II) Complete miscibility (ZrO_2–Y_2O_3). (III) Limited miscibility without a common end-member lattice (ZrO_2–TiO_2). These pseudobinary phase diagrams can be used to predict the formation of interfacial mixed cation structures in the nanolaminates (e.g. YZO in ZrO_2–Y_2O_3 nanolaminates, and the complex (Zr,Ti)-oxide structure in ZrO_2–TiO_2 nanolaminates).

(2) In the absence of nanoepitaxy (pseudomorphic or templated growth), size effects play a significant role in determining the nanocrystalline phases that form within a layer (e.g. t-ZrO_2, t-HfO_2, and o-HfO_2) and at interfaces (e.g. m-(Zr, Ti)O_2). The formation of these phases can be understood in terms of self-assembly into the lowest energy structure in individual critical nuclei.

One future direction is to use these observations to predict the structure of nanolaminates of other oxide partners. For example, consider other combinations of group IVB oxides. ZrO_2 and HfO_2 are completely miscible and isomorphic in lattice structure [67, 70, 76]. Therefore, type II interfaces are

expected to form in a ZrO_2–HfO_2 nanolaminate. In addition, we have shown that the tetragonal phase is the sole structure formed in small ZrO_2 crystallites grown on a physically dissimilar layer (Al_2O_3). A bilayer unit in a ZrO_2–HfO_2 nanolaminate might therefore consist of a t-ZrO_2 template layer followed by a nanoepitaxial t-HfO_2 layer (analogous to templated c-ZYO growth in ZrO_2–Y_2O_3 nanolaminates). The t-ZrO_2 layer would have the function of selecting t-HfO_2 and squelching growth of the o-HfO_2 phase that is observed along with t-HfO_2 in HfO_2–Al_2O_3 nanolaminates. ZrO_2–HfO_2 nanolaminates would also have an additional advantage over HfO_2–Al_2O_3 nanolaminates because they have both a higher refractive index and a higher dielectric constant.

The bulk pseudobinary HfO_2–TiO_2 phase diagram [77] is similar to that of ZrO_2–TiO_2 discussed in section 3.3. Type III interfaces with extended interfacial mixing are therefore expected to form in HfO_2–TiO_2 nanolaminates. Lynch *et al* [21] identified an m-(Hf,Ti)O_2 phase in bulk composites at elevated pressure. A challenge is to produce this phase in HfO_2–TiO_2, analogous to (Zr, Ti)O_2 formation in ZrO_2–TiO_2 nanolaminates due to the Gibbs–Thomson effect.

A second future direction is to better understand mixed cation phase evolution in the case of type III interfaces from a viewpoint of forming a sequence of low energy structures with the constraint of limited diffusion along the growth direction (perpendicular to the substrate). For example, Raman spectroscopy data (section 3.3) showed that the short range order at a ZrO_2-on-TiO_2 surface was characteristic of the following mixed cation (Zr,Ti)-oxide phases (space groups) with increasing Zr flux: rutile ($P4_2/mnm$) → columbite ($Pbcn$) → baddelyite ($P2_1/c$) [78]. The point groups associated with these space groups are directly connected: C_{2h} (baddelyite) → D_{2h} (columbite) → D_{4h} (rutile) [78]. The bulk pseudobinary diagrams of type III interfaces predict that mixed cation structures will form but they do not tell us what their structure is. A question is how we use space group–subgroup relationships to understand (and therefore design) type III interfaces. A similar question was considered by Dubrovinskaia *et al* with respect to phase evolution of Group IVB binary oxides under pressure [19].

Acknowledgments

The author wishes to acknowledge former UW—Milwaukee Chancellor Dr Nancy L Zimpher for providing the funds to set up and maintain the Advanced Coatings Experimental Laboratory (AceLab), where much of this work was carried out.

References

[1] Fehlner F F 1981 *Low Temperature Oxidation* (New York: Wiley–Interscience) chapter 3
[2] Aita C R 1998 *Crit. Rev. Solid State Mater. Sci.* **23** 205
[3] Venables J A, Spiller G D T and Hanbücken M 1984 *Rep. Prog. Phys.* **47** 399
[4] Tromp R M and Hannon J B 2002 *Surf. Rev. Lett.* **9** 1565
[5] Garvie R C 1987 *J. Phys. Chem.* **82** 218
[6] Tu K-N, Mayer J W and Feldman L C 1992 *Electronic Thin Film Science* (New York: Macmillan) pp 100–13
[7] Birkholz M 1995 *Z. Phys.* B **96** 325
Birkholz M 1995 *Z. Phys.* B **96** 333
Ayyab P, Palkar V R, Chattopadhyay S and Multani M 1995 *Phys. Rev.* B **51** 6135
[8] Green D J, Hannink R H J and Swain M V 1989 *Transformation Toughening of Ceramics* (Boca Raton, FL: CRC Press) pp 1–55
[9] Lysenko V A 1994 *Inorg. Mater.* **30** 930
[10] Ruh R, Mazdiyasni K S, Valentine P G and Bielstein H O 1984 *J. Am. Ceram. Soc.* **67** C190
[11] Tuilier M H, Dexpert-Ghys J, Dexpert H and Lagarde P 1987 *J. Solid State Chem.* **69** 153
[12] Pascaul C and Duran P 1982 *J. Am. Ceram. Soc.* **66** 23
[13] Scott H G 1977 *J. Mater. Sci.* **12** 311
Scott H G 1977 *Acta Crystallogr.* B **33** 281
[14] McHale A E and Roth R S 1983 *J. Am. Ceram. Soc.* **66** C-18
McHale A E and Roth R S 1986 *J. Am. Ceram. Soc.* **69** 827
[15] Yamamoto A, Yamada T, Ikawa H, Fukunaga O, Tanaka K and Marumo F 1991 *Acta Crystallogr.* C **47** 1588
[16] Troitzsch U and Ellis D J 2005 *J. Mater. Sci.* **40** 4571
[17] Troitzsch U, Christy A G and Ellis D J 2005 *Phys. Chem. Minerals* **32** 504
[18] Farges F, Brown G E Jr and Rehr J J 1997 *Phys. Rev.* B **56** 1809
[19] Dubrovinskaia N, Dubrovinsky L S, Ahuja R, Prokopenko V B, Dmitriev V, Weber H-P, Osorio-Guillen J and Johansson B 2001 *Phys. Rev. Lett.* **87** 275501
[20] El Goresy A, Chen M, Dubrovinsky L, Gillet P and Graup G 2001 *Science* **293** 1467
[21] Lynch R W and Morosin B 1972 *J. Am. Chem. Soc.* **55** 410
[22] Garvie R S, Hannink R H and Pascoe R T 1975 *Nature* **258** 703
[23] Aita C R 1995 *US Patent Specification* 5472795
[24] Scanlan C M, Gajdardziska-Josifovska M and Aita C R 1994 *Appl. Phys. Lett.* **64** 3548
[25] Aita C R, Wiggins M D, Whig R, Scanlan C M and Gajdardziska-Josifovska M 1996 *J. Appl. Phys.* **79** 1176
[26] Schofield M A, Gajdardziska-Josifovska M, Aita C R and Rice P M 1998 *Thin Solid Films* **326** 106
[27] Gaertner W F, Hoppe E E, Omari M A, Sorbello R S and Aita C R 2004 *J. Vac. Sci. Technol.* A **22** 272
[28] Aita C R, Yakovlev V, Cayton M, Mirhoseini M and Aita M 2005 *US Patent Specification* 6869701
[29] Aita C R, Hoppe E E and Sorbello R S 2003 *Appl. Phys. Lett.* **82** 677
[30] Aita C R, Wiggins M D, Tian B, Scanlan C M and Gajdardziska-Josifovska M 1995 *Elevated Temperature Coatings: Science and Technology I* ed N B Dahotre, J M Hampikian and J J Stiglich (Warrendale: TMS) pp 235–54
[31] See for example: Pawlewicz W T and Hays D D 1984 *Thin Solid Films* **94** 31
[32] Fu X, Clark L A, Yang Q and Anderson M 1996 *Environ. Sci. Technol.* **30** 647
[33] Emeline A, Kataeva G V, Litke A S, Rudakova A V, Ryabchuk V K and Serpone N 1998 *Langmuir* **14** 5011
[34] Emeline A, Kuzmin G N, Purevdorf D, Ryabchuk V K and Serpone N 2002 *J. Phys. Chem.* B **104** 2989
[35] Iacconi P, Lapraz D and Caruba R 1978 *Phys. Status Solidi* a **50** 275
[36] Mikhailov M M and Kuznetsov N Y 1988 *Inorg. Mater.* **24** 656
[37] DeLoach J D and Aita C R 2000 *J. Mater. Sci. Lett.* **19** 1123
[38] Aita C R, DeLoach J D and Sorbello R S 2003 *J. Appl. Phys.* **94** 654
[39] Wilk G D, Wallace R M and Anthony J M 2001 *J. Appl. Phys.* **89** 5243
Robertson J and Falabretti B 2006 *J. Appl. Phys.* **100** 014111
[40] Wang J, Li L P and Stevens R 1992 *J. Mater. Sci* **27** 5397

[41] See for example von Engel A 1965 *Ionized Gases* (London: Claredon)
Chapman B 1980 *Glow Discharge Processes* (New York: Wiley)
[42] Sigmund P 1969 *Phys. Rev.* **184** 383
[43] Aita C R 1993 *J. Vac. Sci. Technol.* A **11** 1540
[44] Kwok C-K and Aita C R 1989 *J. Appl. Phys.* **66** 2756
[45] Bauer E 1964 *Single Crystal Films* ed M H Francombe and H Sato (New York: MacMillan) pp 43–67
[46] Gajdardziska-Josifovska M and Aita C R 1996 *J. Appl. Phys.* **79** 1315
[47] Schofield M A, Gajdardziska-Josifovska M, Aita C R and Rice P M 1998 *Thin Solid Films* **326** 117
[48] Aita C R 1998 *Surf. Eng.* **14** 421
Aita C R 1999 *Surf. Eng.* **15** 195
[49] Bendoraitis J G and Salomon R E 1965 *J. Phys. Chem.* **69** 3666
[50] Kwok C-K and Aita C R 1990 *J. Vac. Sci. Technol.* A **8** 3345
[51] French R H, Glass S J, Ohuchi F S, Xu Y-N and Ching W-Y 1994 *Phys. Rev.* B **49** 5133
[52] Tang H, Levy F, Berger H and Schmid P E 1995 *Phys. Rev.* B **52** 7771
[53] Wells A F 1950 *Structural Inorganic Chemistry* (Oxford: Clarendon) p 35
[54] Tanabe K, Sumiyoshi T, Shibata K, Kiyoura T and Kitagawa J 1974 *Bull. Chem. Soc. Japan* **47** 1064
[55] Kung H H 1984 *J. Solid State Chem.* **52** 191
[56] Wells A F 1950 *Structural Inorganic Chemistry* (Oxford: Clarendon) p 70
[57] Onodera Y and Toyozawa Y 1968 *J. Phys. Soc. Japan* **24** 341
[58] Aita C R, DeLoach J D and Sorbello R S 2002 *Appl. Phys. Lett.* **81** 238
[59] Krebs M A and Cohdrate Sr. R A 1988 *J. Mater. Sci. Lett.* **7** 1327
Zhilin A A, Petrov V I, Tsenter Y and Chuvaeva T I 1992 *Opt. Spectrosc.* **28** 2273
[60] Kim Y K and Jang H M 2001 *J. Appl. Phys.* **89** 6349
[61] Aita C R 2006 *J. Vac. Sci. Technol.* A **24** 2054
[62] Aita C R 2007 *Appl. Phys. Lett.* **90** 213113
[63] Johnson W L 1986 *Prog. Mater. Sci.* **30** 81
[64] Meng W J, Nieh C W and Johnson W L 1986 *Appl. Phys. Lett.* **51** 1693
[65] Shin H, Agarwal M, De Guire M R and Heuer A H 1996 *J. Am. Ceram. Soc.* **79** 1975
[66] DeLoach J D, Shibilski J J, Crape C R and Aita C R 2000 *J. Vac. Sci. Technol.* A **18** 2922
[67] Jaffe J E, Bachorz R A and Gutowski M 2005 *Phys. Rev.* B **72** 114107
[68] Kang J, Lee E-C and Chang K-J 2003 *Phys. Rev.* B **68** 054106
[69] Ohtaka O, Yamanaka T, Kume S, Hara N, Asano H and Izumi F 1995 *J. Am. Ceram. Soc.* **78** 33
[70] Lowther J E, Dewhurst J K, Leger J M and Haines J 1999 *Phys. Rev.* B **60** 14485
[71] Hoppe E E, Sorbello R S and Aita C R 2007 *J. Appl. Phys.* **101** 123534
[72] Hoppe E E, Aita C R and Gajdardziska-Josifovska M 2007 *Appl. Phys. Lett.* **91** 203105
[73] Bohra F, Jiang B and Zuo J-M 2007 *Appl. Phys. Lett.* **90** 161917
[74] Gertsman V Y, Zhilyaev A P and Szpunar J A 1997 *Modelling Simul. Mater. Sci. Eng.* **5** 35
[75] Zheng W, Bowen K H Jr, Li J, Dabkowska I and Gutowski M 2005 *J. Phys. Chem.* **109** 11521
[76] Levin E M and McMurdie H F 1975 *Phase Diagrams for Ceramists* (Westerville: American Ceramic Society) p 166
[77] Coutures J-P and Coutures J 1987 *J. Am. Ceram. Soc.* **70** 383
[78] Giacovazzo C 1992 *Fundamentals of Crystallography* (Oxford: Oxford Science) chapter 1